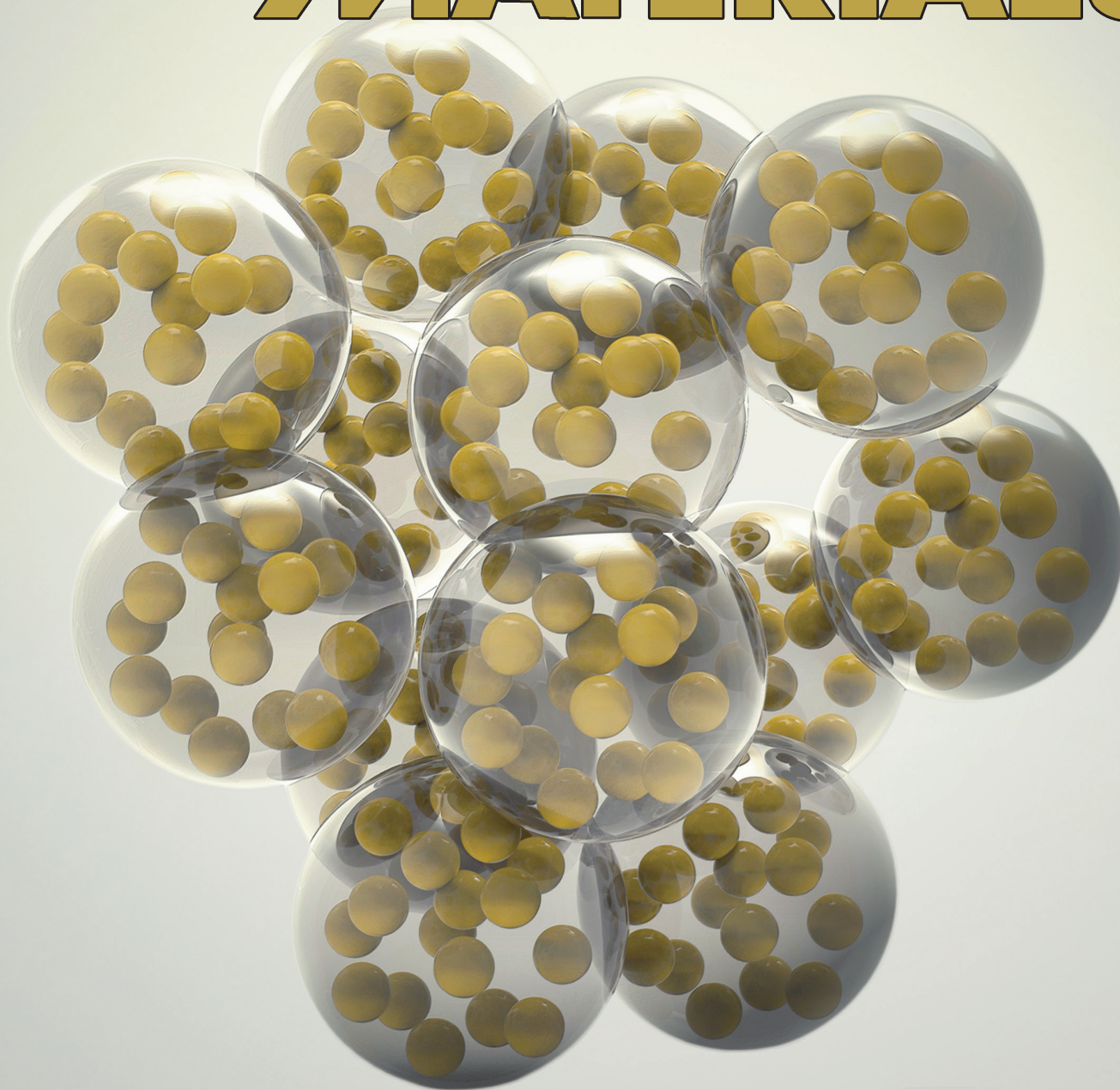


www.advmat.de

ADVANCED MATERIALS



Effect of Carbon Matrix Dimensions on the Electrochemical Properties of $\text{Na}_3\text{V}_2(\text{PO}_4)_3$ Nanograins for High-Performance Symmetric Sodium-Ion Batteries

Shuo Li, Yifan Dong, Lin Xu, Xu Xu, Liang He, and Liqiang Mai*

The urgent demands for developing a sustainable and “green” environment requires the establishment of efficient and low-cost energy storage systems, which will be one of the great challenges in the 21st century and has already attracted extensive attention in our daily life.^[1–4] Among the various available energy storage technologies, lithium-ion batteries play a dominant role in portable electronic devices and have become the prime candidate to power the next generation electric vehicles and plug-in hybrid electric vehicles.^[5–12] Undoubtedly wide-scale implementation of renewable energy will require growth in the production of inexpensive and efficient energy storage systems. However, the increasing demand for lithium (Li) supplies will bring about a steep rise in the Li resources price and consumption in the foreseeable future because the use of lithium-ion batteries has expanded to large-scale applications.^[13–16]

Sodium (Na) is located below Li in the periodic table and shares similar physical and chemical properties with Li in many aspects, thus sodium can be a promising candidate for substituting lithium in rechargeable batteries.^[17–19] Additionally, sodium is optimistically abundant in nature (ranking fourth among the most abundant elements in the Earth crust) and fairly low in cost.^[20–22] All the advantages of sodium support the exploration of sodium-based rechargeable batteries, viz. sodium-ion batteries. Furthermore, many materials as well as design processes currently applied for lithium-ion batteries can also be used in the sodium-ion batteries.^[23–29] And obviously, the sodium-ion batteries explore a new and important direction for energy storage systems.^[30–38]

Despite the numerous advantages of sodium-ion batteries, there still are challenges, for example, in the search for suitable electrode materials for sodium-ion batteries. Because of the larger ionic radius of Na^+ (0.98 Å) in comparison to that of Li^+ (0.69 Å), the diffusion coefficient of Na^+ intercalation into the electrode is more impeditive.^[17,39–42] Besides, the larger Na^+ ions will surely result in severe structure degradation of

electrode materials during the intercalation/deintercalation process. Therefore, the requirements of long cycle life and high rate capability of sodium-ion batteries in energy storage applications should be satisfied. $\text{Na}_3\text{V}_2(\text{PO}_4)_3$ (NVP) is a promising candidate for sodium-ion battery electrodes because it is a typical NASICON (Na super-ionic conductor) type compound.^[43–45] $\text{Na}_3\text{V}_2(\text{PO}_4)_3$ was originally investigated for use as a solid electrolyte that allows fast Na^+ ion conduction through the empty space in its crystal structure.^[46,47] It is built up from isolated $[\text{VO}_6]$ octahedra and $[\text{PO}_4]$ tetrahedrally interlinked via corners to establish the framework anion $[\text{V}_2(\text{PO}_4)_3]^{3-}$. The two independent Na^+ cations are partially occupied and located in channels with two different oxygen environments, viz. six-fold coordination for the first and eightfold for the second Na^+ cation.^[48] This unique structure provides an open, three-dimensional framework that is known for its facile Na^+ ion migration.^[49,50] Besides, $\text{Na}_3\text{V}_2(\text{PO}_4)_3$ has two different voltage plateaus at around 3.3 V and 1.6 V, and therefore this material can be assembled to a symmetrical full battery with an output voltage of 1.7 V. This unique property renders $\text{Na}_3\text{V}_2(\text{PO}_4)_3$ a perfect candidate for application in symmetric batteries with the utilization of the same material for the cathode and the anode simultaneously.^[51–53] However, only a few reports of $\text{Na}_3\text{V}_2(\text{PO}_4)_3$'s performance as battery electrode exist in the literature, and the reversibility and cyclability of $\text{Na}_3\text{V}_2(\text{PO}_4)_3$ need to be enhanced. In addition, the electron and Na^+ ion diffusion pathways in the electrode were not clearly compared and illustrated before.

Herein, a facile synthesis method of $\text{Na}_3\text{V}_2(\text{PO}_4)_3$ nanograins by calcination is described, which can be applied in large-scale production and has great potential in manifold applications. As carbon matrices have a significant influence on the $\text{Na}_3\text{V}_2(\text{PO}_4)_3$ performance, this synthetic route is employed rationally and the $\text{Na}_3\text{V}_2(\text{PO}_4)_3$ nanograins are dispersed in different carbon matrices from zero-dimensional (0D), one-dimensional (1D) to two-dimensional (2D) nanostructures, i.e., acetylene carbon (AC) nanospheres, carbon nanotubes (CNT) and graphite nanosheets by adjusting the carbon source as well as reductant. The influence and mechanism of carbon matrices on the active $\text{Na}_3\text{V}_2(\text{PO}_4)_3$ nanograins are investigated and an explanation is proposed. The electrochemical performances of $\text{Na}_3\text{V}_2(\text{PO}_4)_3$ nanograins in three carbon architectures in sodium half cells are compared, demonstrating that $\text{Na}_3\text{V}_2(\text{PO}_4)_3$ dispersed in the AC nanospheres has the best sodium-ion battery performance (approximately 100% of the theoretical capacity at 0.5 C and 96.4% capacity retention at 5 C after 200 cycles), while in the CNT matrix the performance is moderate, and in the graphite nanosheets the performance is inferior. Furthermore,

S. Li, Ms. Y. F. Dong, Dr. L. Xu, X. Xu, Dr. L. He,
Prof. L. Q. Mai
State Key Laboratory of Advanced Technology
for Materials Synthesis and Processing
WUT-Harvard Joint Nano Key Laboratory
Wuhan University of Technology
Wuhan 430070, P. R. China
E-mail: mlq518@whut.edu.cn

Dr. L. Xu
Department of Chemistry and Chemical Biology
Harvard University, Cambridge
Massachusetts 02138, USA



DOI: 10.1002/adma.201305522

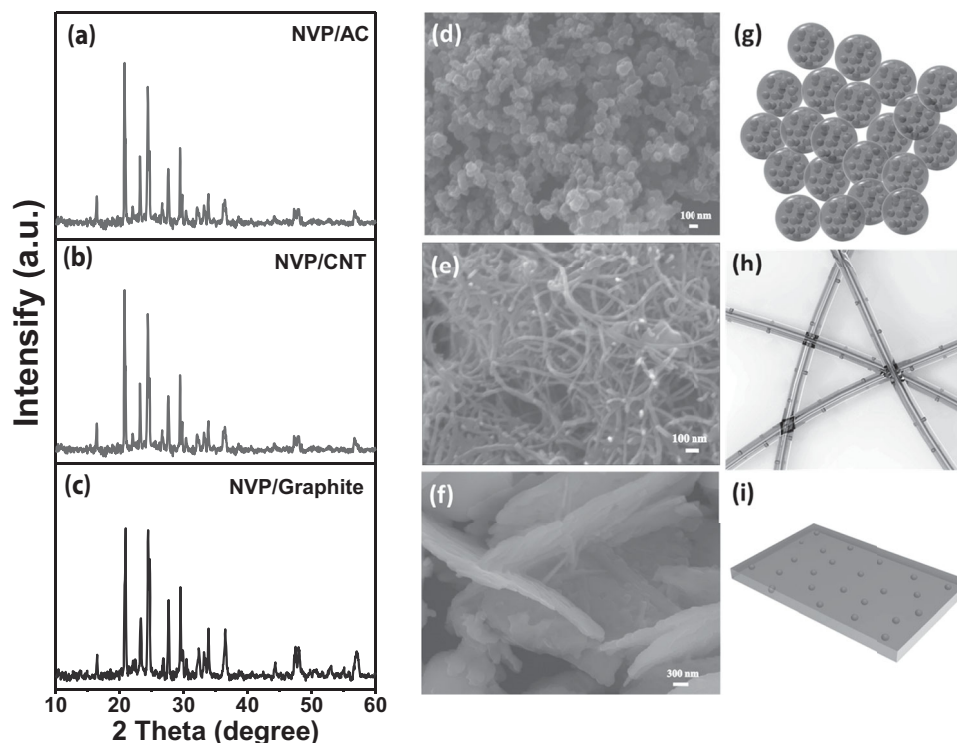


Figure 1. XRD patterns, SEM images and schematic illustrations of $\text{Na}_3\text{V}_2(\text{PO}_4)_3/\text{AC}$ (a,d,g), $\text{Na}_3\text{V}_2(\text{PO}_4)_3/\text{CNT}$ (b,e,h) and $\text{Na}_3\text{V}_2(\text{PO}_4)_3/\text{graphite}$ (c,f,i), respectively.

a high-performance symmetric sodium-ion battery that exploits the unique electrode characteristics is assembled and the battery offers excellent performance, which has never been reported before. The symmetric battery can be cycled at a 10 C rate with minor decays in capacity when recovered, and it has an unusual cycling stability: exceeding 200 cycles at a 1 C rate with no substantial losses in capacity delivery. The performances of $\text{Na}_3\text{V}_2(\text{PO}_4)_3$ nanograins in different matrices from 0D to 3D nanostructures are also compared in symmetric full sodium-ion batteries, and the performance shows the same trends as in sodium half batteries.

Figure 1a–c depict the X-ray diffraction patterns (XRD) of the as-synthesized $\text{Na}_3\text{V}_2(\text{PO}_4)_3$ nanograins dispersed in different carbon matrices. The characteristic peaks of different samples can be readily indexed to a well-defined NASICON structure in a $P2_1/n$ space group (monoclinic unit cell) with $a = 8.566 \text{ \AA}$ and $b = 12.053 \text{ \AA}$. These values correspond well with the existing values in literatures.^[45,54] The morphologies of $\text{Na}_3\text{V}_2(\text{PO}_4)_3/\text{AC}$, $\text{Na}_3\text{V}_2(\text{PO}_4)_3/\text{CNT}$ and $\text{Na}_3\text{V}_2(\text{PO}_4)_3/\text{graphite}$ are characterized by field-emission scanning electron microscopic (FESEM) images in **Figure 1d–f** with regular shapes and a narrow size distribution, respectively. The morphologies of $\text{Na}_3\text{V}_2(\text{PO}_4)_3/\text{AC}$, $\text{Na}_3\text{V}_2(\text{PO}_4)_3/\text{CNT}$ and $\text{Na}_3\text{V}_2(\text{PO}_4)_3/\text{graphite}$ are similar to their carbon matrices when compared with the SEM images of the corresponding carbon matrices in **Figure S1**. This phenomenon is attributed to the fact that the carbon sources act as templates in synthesis process to control the morphology. **Figure 1g–i** are the schematic illustrations of our as-synthesized $\text{Na}_3\text{V}_2(\text{PO}_4)_3$ nanograins in different carbon networks. The carbon templates form conductive networks for electron

transport, thus promoting the conductivity of $\text{Na}_3\text{V}_2(\text{PO}_4)_3$. Energy dispersive X-ray spectrometry (EDS) mapping analyses of different samples (**Figure S2a–c**) unambiguously confirm that $\text{Na}_3\text{V}_2(\text{PO}_4)_3$ nanograins are homogeneously dispersed in AC, CNT and graphite networks, resulting in improved electrical conductivity. The carbon amount in each sample is determined by element analysis, and the carbon contents are 8.46%, 8.37%, and 8.54% for $\text{Na}_3\text{V}_2(\text{PO}_4)_3/\text{AC}$, $\text{Na}_3\text{V}_2(\text{PO}_4)_3/\text{CNT}$ and $\text{Na}_3\text{V}_2(\text{PO}_4)_3/\text{graphite}$, respectively. This indicates that the carbon contents in the three samples are almost same. Nitrogen sorption isotherms were generated to investigate the Brunauer–Emmet–Teller (BET) surface area of the samples (**Figure S3**). The $\text{Na}_3\text{V}_2(\text{PO}_4)_3/\text{AC}$ has the largest BET surface area, which is about $25 \text{ m}^2 \text{ g}^{-1}$. The surface area of the $\text{Na}_3\text{V}_2(\text{PO}_4)_3/\text{CNT}$ is less, about $12 \text{ m}^2 \text{ g}^{-1}$. And the $\text{Na}_3\text{V}_2(\text{PO}_4)_3/\text{graphite}$ has the smallest surface area, which is only $4 \text{ m}^2 \text{ g}^{-1}$. This result shows that $\text{Na}_3\text{V}_2(\text{PO}_4)_3/\text{AC}$ has the largest contact area with the electrolyte during cycling.

Transmission electron microscopy (TEM) was utilized to characterize the morphologies and obtain detailed structures of the products. **Figure 2a** indicates that the $\text{Na}_3\text{V}_2(\text{PO}_4)_3$ nanograins are well dispersed in AC nanospheres, which have a physical morphology of finely divided pellets and form a 3D conductive network. **Figure 2b** is a high-resolution (HR) TEM image of $\text{Na}_3\text{V}_2(\text{PO}_4)_3/\text{AC}$, in which $\text{Na}_3\text{V}_2(\text{PO}_4)_3$ are nanograins with a diameter of $\sim 5 \text{ nm}$. The lattice fringes of $\text{Na}_3\text{V}_2(\text{PO}_4)_3$ are clear, indicating its high crystallinity. The morphology of AC particles is sphere-like and surround the $\text{Na}_3\text{V}_2(\text{PO}_4)_3$ nanograins, and the lattice fringes of AC can also be detected and the interface between $\text{Na}_3\text{V}_2(\text{PO}_4)_3$ and AC can be easily observed. For

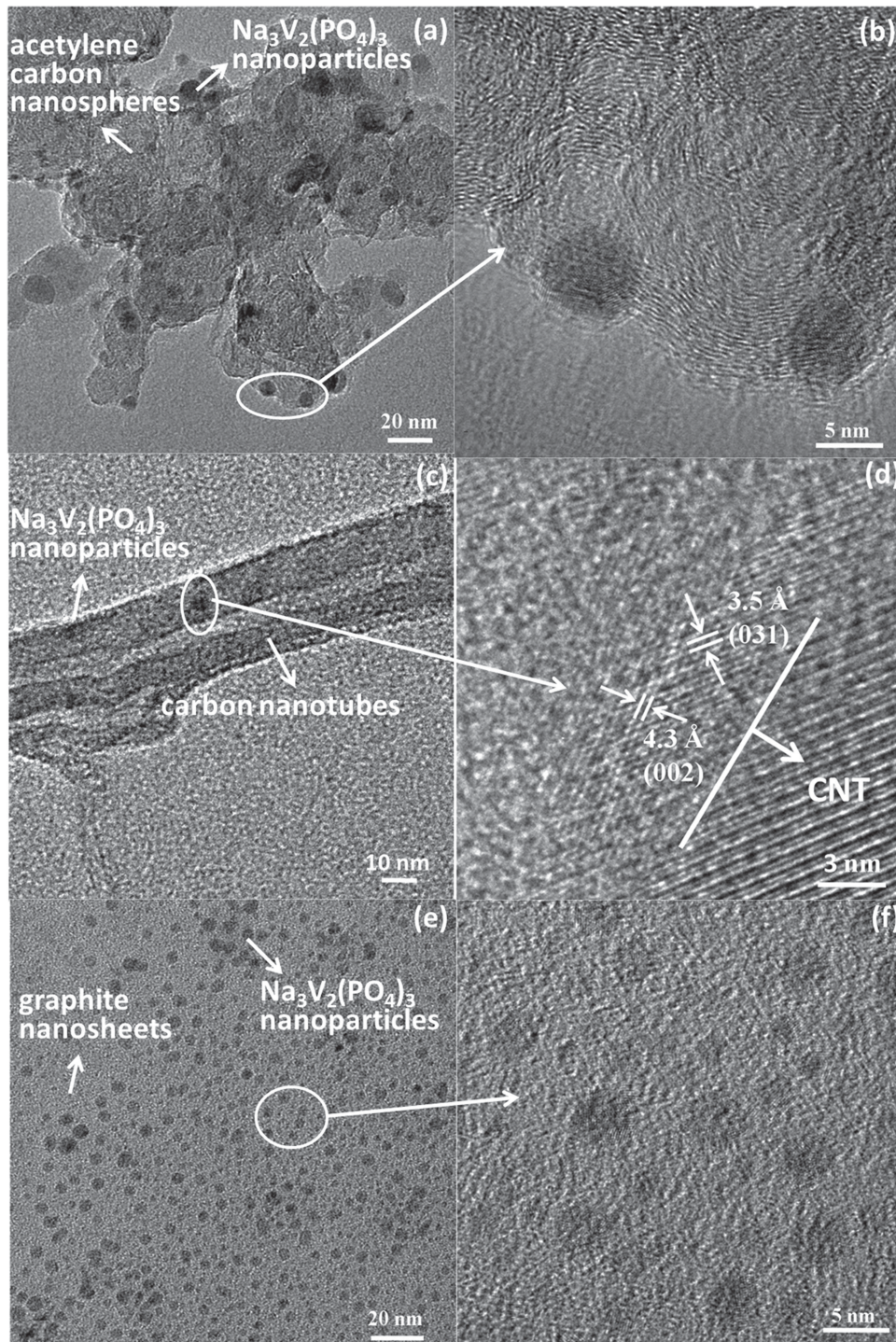


Figure 2. TEM and HRTEM images of $\text{Na}_3\text{V}_2(\text{PO}_4)_3/\text{AC}$ (a,b), $\text{Na}_3\text{V}_2(\text{PO}_4)_3/\text{CNT}$ (c,d) and $\text{Na}_3\text{V}_2(\text{PO}_4)_3/\text{graphite}$ (e,f), respectively.

$\text{Na}_3\text{V}_2(\text{PO}_4)_3/\text{CNT}$, the $\text{Na}_3\text{V}_2(\text{PO}_4)_3$ nanograins are dispersed on the CNT, as indicated in Figure 2c. Combined with the EDS mapping in Figure S2b, it can be deduced that the $\text{Na}_3\text{V}_2(\text{PO}_4)_3$ are uniformly dispersed in the CNT matrix. The HRTEM image of $\text{Na}_3\text{V}_2(\text{PO}_4)_3/\text{CNT}$ (Figure 2d) shows clear lattice fringes of $\text{Na}_3\text{V}_2(\text{PO}_4)_3$ and CNT, the width of 4.3 and 3.5 Å between neighboring lattice fringes of $\text{Na}_3\text{V}_2(\text{PO}_4)_3$ correspond to the

(002) and (031) planes of $\text{Na}_3\text{V}_2(\text{PO}_4)_3$, respectively. The lattice fringes of $\text{Na}_3\text{V}_2(\text{PO}_4)_3$ nanograins confirm the pure crystalline phase of these nanoparticles. The TEM and HRTEM images (Figure 2e and 2f) of $\text{Na}_3\text{V}_2(\text{PO}_4)_3/\text{graphite}$ show that the $\text{Na}_3\text{V}_2(\text{PO}_4)_3$ nanograins are distributed in the graphite nanosheets, and the particle sizes of the nanograins are ~5 nm with good crystallinity. The graphite nanosheets are

two-dimensional and the boundaries between the $\text{Na}_3\text{V}_2(\text{PO}_4)_3$ nanograins and graphite are clearly observed. The size of $\text{Na}_3\text{V}_2(\text{PO}_4)_3$ nanograins in different carbon matrices are all maintained at 5 nm and it is remarkable that the structures are kept well-defined nanosized morphology through the calcinations at 800 °C. The lattice fringes of different carbonaceous materials can also be observed in the corresponding HRTEM images, indicating that all the carbon matrices are crystallized. The spacings of the carbon matrices are nearly 3.3 Å, well consistent with the previous reported crystalline carbon interlayer spacing (3.35 Å). It can be seen that in all the TEM images of $\text{Na}_3\text{V}_2(\text{PO}_4)_3/\text{AC}$, $\text{Na}_3\text{V}_2(\text{PO}_4)_3/\text{CNT}$ and $\text{Na}_3\text{V}_2(\text{PO}_4)_3/\text{graphite}$, the $\text{Na}_3\text{V}_2(\text{PO}_4)_3$ nanograins are intimately interconnected by carbon bridges. The carbon bridges act as electron pathways that electrically interconnect the $\text{Na}_3\text{V}_2(\text{PO}_4)_3$ nanograins, ultimately providing the electrode with a very high conductivity. Also the Na^+ ion diffusion lengths are reduced by the nanoscale diameter of $\text{Na}_3\text{V}_2(\text{PO}_4)_3$, thus offering excellent kinetics for Na^+ intercalation/deintercalation process.

The electrochemical performance of $\text{Na}_3\text{V}_2(\text{PO}_4)_3/\text{AC}$, $\text{Na}_3\text{V}_2(\text{PO}_4)_3/\text{CNT}$ and $\text{Na}_3\text{V}_2(\text{PO}_4)_3/\text{graphite}$ were characterized

by using CR2025 coin cells with sodium metal as the counter electrode. The discharge voltage of carbonaceous materials is below 1.0 V, therefore the reversible capacity of carbon in the composites is negligible.^[55] The redox couple properties of the $\text{Na}_3\text{V}_2(\text{PO}_4)_3/\text{AC}$, $\text{Na}_3\text{V}_2(\text{PO}_4)_3/\text{CNT}$ and $\text{Na}_3\text{V}_2(\text{PO}_4)_3/\text{graphite}$ cathodes are demonstrated by cyclic voltammetry (CV) curves in Figure 3a for the initial cycle at a scan rate of 0.1 mV s^{-1} in a voltage range of 2.3 to 3.9 V vs. Na/Na^+ . It is obvious that $\text{Na}_3\text{V}_2(\text{PO}_4)_3/\text{AC}$ has larger curve area and higher redox peak current than other samples, indicating that $\text{Na}_3\text{V}_2(\text{PO}_4)_3/\text{AC}$ has the highest capacity and the fastest kinetics for Na^+ ion insertion/extraction. Each sample has an oxidation peak and a reduction peak as shown in Figure 3a. The oxidation (Na extraction) and reduction (Na insertion) peaks are located near 3.3 and 3.5 V. The average voltage is 3.4 V vs. Na/Na^+ , which is close to the equilibrium voltage of $\text{V}^{++}/\text{V}^{3+}$ ($\text{Na}_{1+x}\text{V}_2(\text{PO}_4)_3$, $0 \leq x \leq 2$) redox couple in our as-synthesized materials.^[53] There exist peak shifts in the $\text{Na}_3\text{V}_2(\text{PO}_4)_3/\text{CNT}$ and $\text{Na}_3\text{V}_2(\text{PO}_4)_3/\text{graphite}$ samples: the oxidation peak moves to higher potential and the reduction peak moves to lower potential, resulting in the larger potential difference. This may be attributed to the lower kinetics

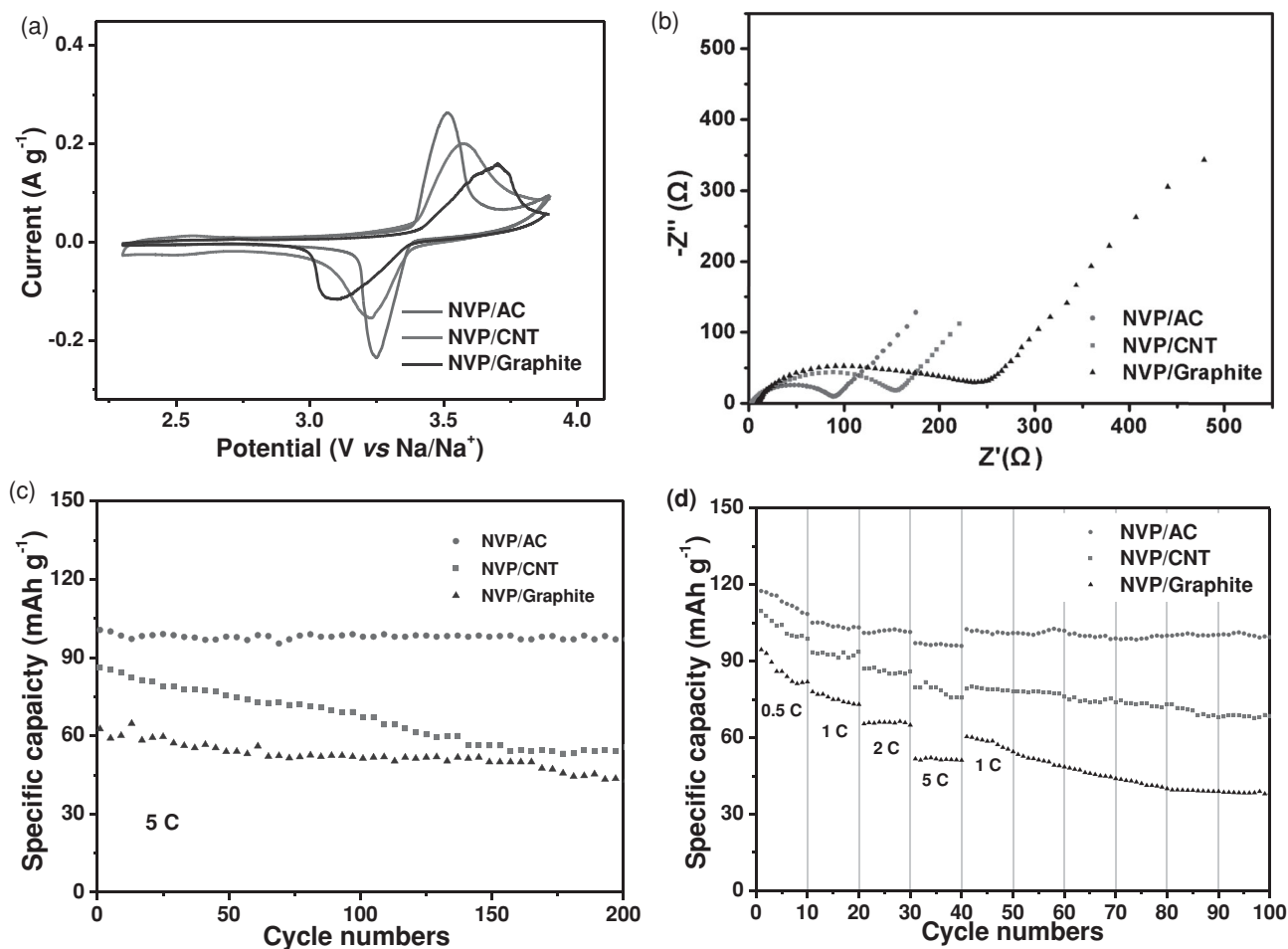


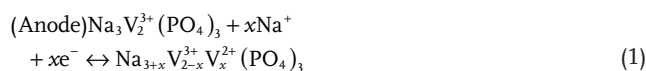
Figure 3. Electrochemical characterizations of $\text{Na}_3\text{V}_2(\text{PO}_4)_3/\text{AC}$, $\text{Na}_3\text{V}_2(\text{PO}_4)_3/\text{CNT}$ and $\text{Na}_3\text{V}_2(\text{PO}_4)_3/\text{graphite}$ cathodes in sodium half cells. (a) Cyclic voltammograms at a scan rate of 0.1 mV s^{-1} in a voltage range of 2.3–3.9 V; (b) Alternating-current impedance plots of the three samples from 0.01 Hz to 100 kHz; (c) Cycling performance of the three samples cycled at 5 C in 2.3–3.9 V for 200 cycles; (d) Rate performance at various current rates from 0.5 C to 5 C, respectively.

of the two samples, thus leading to electrode polarization during cycling. The peak area of $\text{Na}_3\text{V}_2(\text{PO}_4)_3/\text{AC}$ is the largest, indicating $\text{Na}_3\text{V}_2(\text{PO}_4)_3/\text{AC}$ with the largest electrochemical surface area has the best performance of the electrodes. The discharge profiles of the samples at the rate of 1 C (1 C corresponds to 117.6 mA g^{-1}) over a potential window of 2.3 to 3.9 V are presented in Figure S4. It can be clearly seen that all the samples have a flat discharge voltage plateau around 3.3 V, corresponding well with the reduction peaks in the CV curve. This is identified as the phase transition process of the extraction of almost 1.7 atoms of sodium per formula unit. The initial specific discharge capacity of $\text{Na}_3\text{V}_2(\text{PO}_4)_3/\text{AC}$ is 108.9 mAh g^{-1} , higher than 94.8 and 67.1 mAh g^{-1} for $\text{Na}_3\text{V}_2(\text{PO}_4)_3/\text{CNT}$ and $\text{Na}_3\text{V}_2(\text{PO}_4)_3/\text{graphite}$, respectively. Electrochemical impedance spectroscopic (EIS) measurements were carried out in order to compare the conductivity and diffusion ability of the as-synthesized $\text{Na}_3\text{V}_2(\text{PO}_4)_3/\text{AC}$, $\text{Na}_3\text{V}_2(\text{PO}_4)_3/\text{CNT}$ and $\text{Na}_3\text{V}_2(\text{PO}_4)_3/\text{graphite}$ electrodes (Figure 3b). The entire Nyquist plots exhibit a semicircle in the high-frequency region and a straight line in the low-frequency region. The semicircle is ascribed to the Na^+ ion migration through the interface between the surface layer of the particles and the electrolyte. By comparing the charge-transfer resistance (R_{ct}), it is found that the R_{ct} of $\text{Na}_3\text{V}_2(\text{PO}_4)_3/\text{graphite}$ is the highest, followed by $\text{Na}_3\text{V}_2(\text{PO}_4)_3/\text{CNT}$, and $\text{Na}_3\text{V}_2(\text{PO}_4)_3/\text{AC}$ has the lowest resistance. This may be ascribed to the much larger carbon matrix size of graphite and the inhomogeneity of $\text{Na}_3\text{V}_2(\text{PO}_4)_3$ particle size in graphite matrix as indicated in Figure 1f and 2f. The straight line is attributed to the diffusion of sodium ions in the bulk of the electrode material, and the diffusion coefficient value (D) of the sodium ions can be calculated using the equation $D = 0.5(RT/AF^2\sigma_w C)^2$, where R is the gas constant, T is the temperature, A is the area of the electrode surface, F is the Faraday's constant, σ_w is the Warburg factor, and C is the molar concentration of Na^+ ions.^[56] The calculated sodium diffusion coefficient values for $\text{Na}_3\text{V}_2(\text{PO}_4)_3/\text{AC}$, $\text{Na}_3\text{V}_2(\text{PO}_4)_3/\text{CNT}$ and $\text{Na}_3\text{V}_2(\text{PO}_4)_3/\text{graphite}$ are 1.51×10^{-12} , 1.38×10^{-12} and $1.26 \times 10^{-12} \text{ cm}^2 \text{ s}^{-1}$, respectively. It can be found that the sodium diffusion coefficient of $\text{Na}_3\text{V}_2(\text{PO}_4)_3/\text{AC}$ possesses the highest value, indicating the fastest Na^+ ions transport in $\text{Na}_3\text{V}_2(\text{PO}_4)_3/\text{AC}$.

It can be concluded from the above electrochemical analyses that the $\text{Na}_3\text{V}_2(\text{PO}_4)_3/\text{AC}$ has the best electrochemical performance, and this is subsequently verified. The cyclic performances of the $\text{Na}_3\text{V}_2(\text{PO}_4)_3/\text{AC}$, $\text{Na}_3\text{V}_2(\text{PO}_4)_3/\text{CNT}$ and $\text{Na}_3\text{V}_2(\text{PO}_4)_3/\text{graphite}$ electrodes in 2.3 to 3.9 V at 5 C rate are demonstrated in Figure 3c. The initial discharge capacity of $\text{Na}_3\text{V}_2(\text{PO}_4)_3/\text{AC}$ cathode is up to 100.6 mAh g^{-1} , closer to the theoretical capacity than the other two samples. This value is much higher than 86.2 mAh g^{-1} for $\text{Na}_3\text{V}_2(\text{PO}_4)_3/\text{CNT}$ and 62.6 mAh g^{-1} for $\text{Na}_3\text{V}_2(\text{PO}_4)_3/\text{graphite}$. After 200 cycles, the capacities of $\text{Na}_3\text{V}_2(\text{PO}_4)_3/\text{AC}$, $\text{Na}_3\text{V}_2(\text{PO}_4)_3/\text{CNT}$ and $\text{Na}_3\text{V}_2(\text{PO}_4)_3/\text{graphite}$ cathodes decrease to 97.0 , 56.3 and 40.8 mAh g^{-1} , corresponding to the capacity retention of 96.4%, 65.3% and 65.1% of their initial capacity, respectively. It is of great significance that the $\text{Na}_3\text{V}_2(\text{PO}_4)_3/\text{AC}$ possesses almost no capacity fading during cycling, compares well with the commercial lithium-ion batteries and exceeds most of the other rechargeable batteries. For further evaluation of the advantages of the $\text{Na}_3\text{V}_2(\text{PO}_4)_3/\text{AC}$ cathode, rate performance

at progressively increased current densities (ranging from 0.5 C to 5 C) was measured (Figure 3d). The initial discharge capacity of $\text{Na}_3\text{V}_2(\text{PO}_4)_3/\text{AC}$ at 0.5 C is 117.5 mAh g^{-1} in the initial stage, approximately 100% of the theoretical capacity of $\text{Na}_3\text{V}_2(\text{PO}_4)_3$. Note that the formation of a polymeric gel-like film, the decomposition of the electrolyte solution or the possibly interfacial lithium storage may contribute slightly to the initial capacity.^[57] This is further testified by the discharge profile of $\text{Na}_3\text{V}_2(\text{PO}_4)_3/\text{AC}$ at the rate of 0.1 C as indicated in Figure S5. The discharge capacity is 119.6 mAh g^{-1} , slightly larger than the theoretical value of $\text{Na}_3\text{V}_2(\text{PO}_4)_3$ (117.6 mAh g^{-1}). The discharge potential shown in Figure S5 is around 3.35 V, corresponding well with the $\text{Na}_3\text{V}_2(\text{PO}_4)_3$ in previously reported literatures.^[51,58] The discharge capacities of 105.1 , 101.1 and 97.0 mAh g^{-1} are obtained at 1 C, 2 C and 5 C for $\text{Na}_3\text{V}_2(\text{PO}_4)_3/\text{AC}$, respectively. The performance of $\text{Na}_3\text{V}_2(\text{PO}_4)_3/\text{AC}$ at 5 C is much better than that of $\text{Na}_3\text{V}_2(\text{PO}_4)_3/\text{CNT}$ and $\text{Na}_3\text{V}_2(\text{PO}_4)_3/\text{graphite}$ at the same rate, which are only 79.8 and 51.7 mAh g^{-1} , respectively. Even suffering from rapid changes of the current densities, the $\text{Na}_3\text{V}_2(\text{PO}_4)_3/\text{AC}$ electrode exhibits stable capacity at each current. Note that the capacity decay at a current rate of 5 C is slower than that at 0.5 C. This phenomenon may be attributed to the severe degradation, partial dissolution of electrode materials in electrolyte, larger metallic sodium consumption and more side reactions at initial cycles under lower current rates.^[34,41,52] When the current is turned back to 1 C, about 99.3% of the capacity is recovered and there is no obvious capacity loss (only 3.0%) after the subsequent 60 cycles. This rate performance investigation indicates the excellent structural stability and rate capability of $\text{Na}_3\text{V}_2(\text{PO}_4)_3$ nanograins in AC matrix.

It is reported that $\text{Na}_3\text{V}_2(\text{PO}_4)_3$ has electrochemical activity at a lower voltage.^[51,53] The CV curve of $\text{Na}_3\text{V}_2(\text{PO}_4)_3/\text{AC}$ for the initial cycle at a scanning rate of 0.1 mV s^{-1} in a voltage range of 1.3 to 2.0 V vs. Na/Na^+ is shown in Figure S6. Two peaks corresponding to $\text{V}^{3+}/\text{V}^{2+}$ redox couple could be observed, and the average voltage is 1.65 V, and this property endows $\text{Na}_3\text{V}_2(\text{PO}_4)_3$ a candidate to perform as anode. Taking advantage of the big voltage difference between the plateaus, a symmetric cell using $\text{Na}_3\text{V}_2(\text{PO}_4)_3/\text{C}$ as both negative and positive electrodes can be designed.^[53] As expected from the respective voltages at 3.40 and 1.65 V, the combination of $\text{Na}_3\text{V}_2(\text{PO}_4)_3/\text{AC}$ as both cathode and anode gives rise to a battery operating around 1.75 V. Therefore a symmetric sodium-ion battery with structure as $\text{NVP} \parallel 1 \text{ M NaClO}_4/\text{EC} + \text{DMC} \parallel \text{NVP}$ was assembled as shown in Figure S7. Figure S8a shows the CV curve of the symmetric cell at a scan rate of 0.1 mV s^{-1} in the potential range of 1.0 to 3.0 V. Two peaks located at 1.80 and 1.70 V are observed, and the average voltage is 1.75 V, matching well with the expectation. The corresponding voltage profiles of the charge-discharge curves at 1 C of the symmetric battery are shown in Figure S8b (the battery is cathode limited). The discharge capacity and charge capacity are 99.2 and 104.2 mAh g^{-1} , respectively, with an initial coulombic efficiency of 95.2%. The reactions in the symmetric battery can be described as follows:



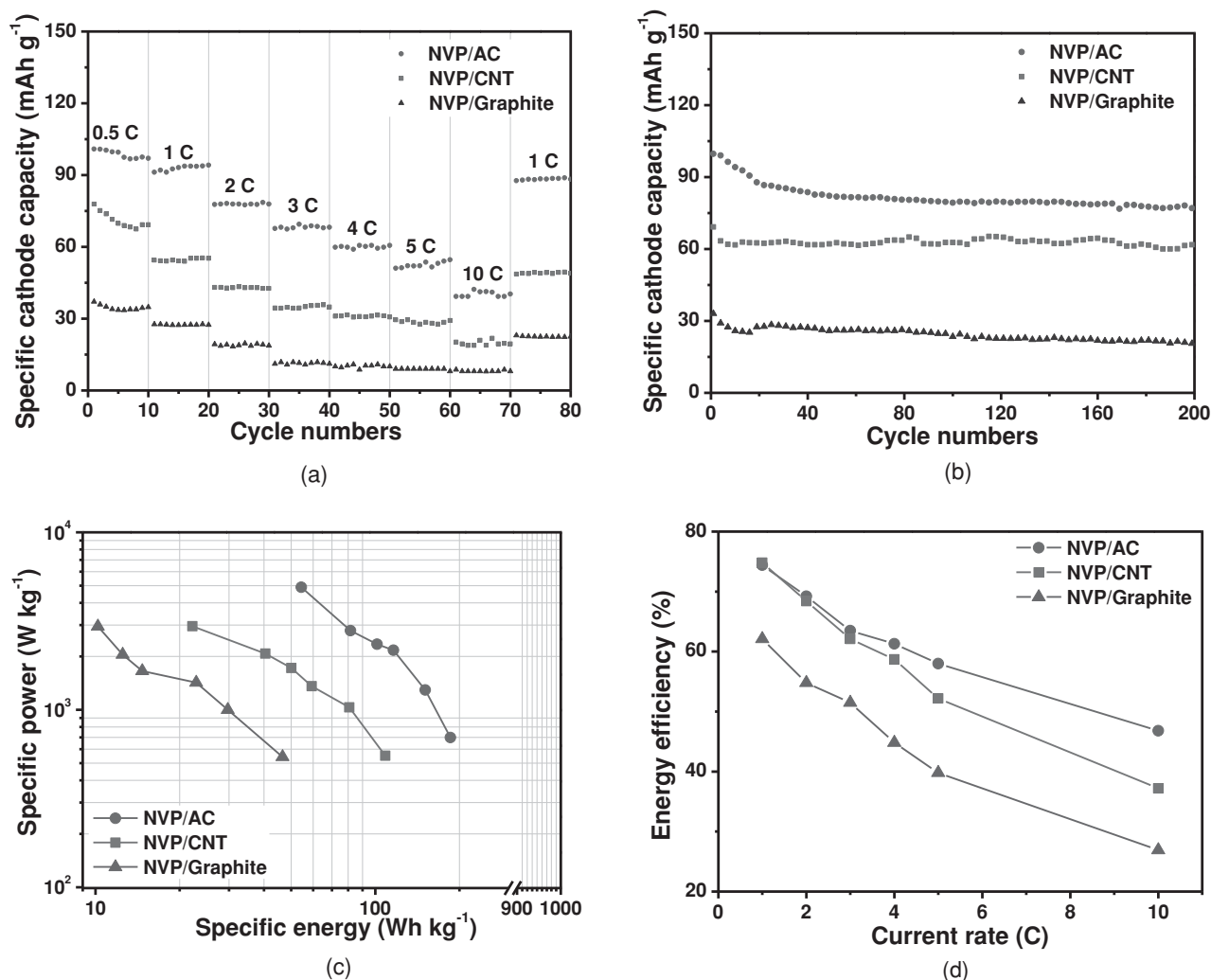
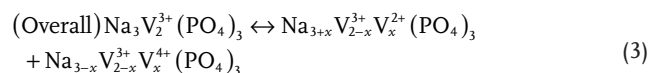
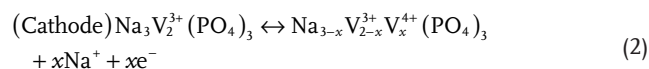


Figure 4. Performances of $\text{Na}_3\text{V}_2(\text{PO}_4)_3/\text{AC}$, $\text{Na}_3\text{V}_2(\text{PO}_4)_3/\text{CNT}$ and $\text{Na}_3\text{V}_2(\text{PO}_4)_3/\text{graphite}$ in symmetric sodium-ion batteries. (a) Rate performance of $\text{Na}_3\text{V}_2(\text{PO}_4)_3/\text{AC}$, $\text{Na}_3\text{V}_2(\text{PO}_4)_3/\text{CNT}$ and $\text{Na}_3\text{V}_2(\text{PO}_4)_3/\text{graphite}$ at various current rates from 0.5 C to 1 C; (b) Cycling performance of $\text{Na}_3\text{V}_2(\text{PO}_4)_3/\text{AC}$, $\text{Na}_3\text{V}_2(\text{PO}_4)_3/\text{CNT}$ and $\text{Na}_3\text{V}_2(\text{PO}_4)_3/\text{graphite}$ cycled at 1 C in 1.0–3.0 V for 200 cycles; (c) Ragone plots of $\text{Na}_3\text{V}_2(\text{PO}_4)_3/\text{AC}$, $\text{Na}_3\text{V}_2(\text{PO}_4)_3/\text{CNT}$ and $\text{Na}_3\text{V}_2(\text{PO}_4)_3/\text{graphite}$ in symmetric sodium-ion batteries; (d) Round-trip energy efficiency of $\text{Na}_3\text{V}_2(\text{PO}_4)_3/\text{AC}$, $\text{Na}_3\text{V}_2(\text{PO}_4)_3/\text{CNT}$ and $\text{Na}_3\text{V}_2(\text{PO}_4)_3/\text{graphite}$ in symmetric sodium-ion batteries.



Rate capability measurement was firstly used to evaluate the symmetric battery performance. As shown in **Figure 4a**, the symmetric batteries with $\text{Na}_3\text{V}_2(\text{PO}_4)_3/\text{AC}$, $\text{Na}_3\text{V}_2(\text{PO}_4)_3/\text{CNT}$ and $\text{Na}_3\text{V}_2(\text{PO}_4)_3/\text{graphite}$ as both electrodes were cycled from 0.5 C to 10 C (58.8 mA g^{-1} to 1176 mA g^{-1}) in the potential range of 1.0 to 3.0 V. The symmetric battery using $\text{Na}_3\text{V}_2(\text{PO}_4)_3/\text{AC}$ electrodes delivers 100.9 mAh g^{-1} at 0.5 C based on the cathode weight, significantly larger than 77.9 mAh g^{-1} for $\text{Na}_3\text{V}_2(\text{PO}_4)_3/\text{CNT}$ and 37.1 mAh g^{-1} for $\text{Na}_3\text{V}_2(\text{PO}_4)_3/\text{graphite}$. The symmetric battery also shows excellent cyclic stability

and the discharge capacity is 94.1, 78.5, 69.4, 60.6 and 54.6 mAh g^{-1} at 1 C, 2 C, 3 C, 4 C, and 5 C, respectively. Even at much higher rate of 10 C, the discharge capacity is 42.2 mAh g^{-1} , and nearly 42% of the initial capacity can be retained. This value of $\text{Na}_3\text{V}_2(\text{PO}_4)_3/\text{AC}$ at 10 C is 2.3 times higher than that of $\text{Na}_3\text{V}_2(\text{PO}_4)_3/\text{CNT}$ and 5.3 times higher than that of $\text{Na}_3\text{V}_2(\text{PO}_4)_3/\text{graphite}$ in symmetric sodium-ion batteries under the same rate, respectively, which is significantly advantageous. Remarkably, when the current density is recovered to 1 C, 94.4% of the capacity can be maintained for $\text{Na}_3\text{V}_2(\text{PO}_4)_3/\text{AC}$ symmetric battery, demonstrating its excellent battery stability. The superior long life of the symmetric batteries was further investigated by testing the same symmetric battery at 1 C for 200 cycles. As shown in **Figure 4b**, the $\text{Na}_3\text{V}_2(\text{PO}_4)_3/\text{AC}$ delivers the highest capacity and that of $\text{Na}_3\text{V}_2(\text{PO}_4)_3/\text{graphite}$ is the lowest. The capacity retention of $\text{Na}_3\text{V}_2(\text{PO}_4)_3/\text{AC}$ symmetric battery is approximately 80% after 200 cycles, which has

never been reported before. The specific energy and specific power of $\text{Na}_3\text{V}_2(\text{PO}_4)_3/\text{AC}$, $\text{Na}_3\text{V}_2(\text{PO}_4)_3/\text{CNT}$ and $\text{Na}_3\text{V}_2(\text{PO}_4)_3/\text{graphite}$ are shown in the Ragone plot (Figure 4c), respectively. The specific energy and specific power was calculated on the basis of the cathode. The $\text{Na}_3\text{V}_2(\text{PO}_4)_3/\text{AC}$ exhibits the highest specific energy of 185.5 Wh kg^{-1} at 1 C, and remarkably, it can deliver a specific power of $\sim 5000 \text{ W kg}^{-1}$. This shows that our symmetric battery has a comparable specific power and energy density, and can be a promising candidate for energy storage systems with both high-power and high-energy densities. The energy efficiency of the $\text{Na}_3\text{V}_2(\text{PO}_4)_3/\text{AC}$ symmetric sodium-ion battery is $\sim 75\%$ at 1 C (Figure 4d), which is better than those of $\text{Na}_3\text{V}_2(\text{PO}_4)_3/\text{CNT}$ and $\text{Na}_3\text{V}_2(\text{PO}_4)_3/\text{graphite}$, and higher than $\sim 70\%$ of redox-flow batteries.^[59] At the rate of 10 C, the energy efficiency can significantly maintain at $\sim 50\%$. It can be expected that the application of the symmetric batteries will demonstrate great potential in the development of energy storage systems due to the several advantages such as improved safety, long preservation, ability of charging in both directions, and low cost because of the utilization of the same material for the cathode and the anode.

Note that the $\text{Na}_3\text{V}_2(\text{PO}_4)_3/\text{AC}$ material delivers the best electrochemical performance in all the battery measurements. It can be concluded that this phenomenon can be attributed to the morphology of the different carbon matrices.^[60] Firstly, it is clear from the BET surface area measurements that $\text{Na}_3\text{V}_2(\text{PO}_4)_3/\text{AC}$ exhibits the largest surface area. The large surface area enables $\text{Na}_3\text{V}_2(\text{PO}_4)_3/\text{AC}$ more contact area with the electrolyte, and this can facilitate electrochemical reactions and efficient penetration of the electrolyte into the active materials, endowing $\text{Na}_3\text{V}_2(\text{PO}_4)_3/\text{AC}$ with reduced Na^+ ion diffusion length, thus resulting in improved electrochemical kinetics. The sodium diffusion coefficient values calculated from EIS measurements also exhibit that the $\text{Na}_3\text{V}_2(\text{PO}_4)_3/\text{AC}$ sample has the best Na^+ ion diffusion ability. Besides, according to the diffusion formula $t = L^2/D$ (where t is the diffusion time, L is the diffusion length and D is the diffusion constant), the shorter diffusion length will provide shorter diffusion time, leading to better electrochemical property. As the size of the AC nanospheres is only several tens of nanometers (Figure S1a), the Na^+ ions can diffuse through the carbon matrix and intercalate into the $\text{Na}_3\text{V}_2(\text{PO}_4)_3$ via relatively shorter pathways in all directions, viz. the Na^+ ion intercalation pathways are three-dimensional in $\text{Na}_3\text{V}_2(\text{PO}_4)_3/\text{AC}$. While for $\text{Na}_3\text{V}_2(\text{PO}_4)_3/\text{CNT}$ and $\text{Na}_3\text{V}_2(\text{PO}_4)_3/\text{graphite}$, the diffusion distances are much longer due to the larger size and more dimensions of carbon matrices and less contact areas with the electrolyte. This means that the diffusion length in the AC is the shortest, thus providing $\text{Na}_3\text{V}_2(\text{PO}_4)_3/\text{AC}$ the fastest Na^+ ion diffusion and the best performance. In addition, as it is identified that the active material $\text{Na}_3\text{V}_2(\text{PO}_4)_3$ is dispersed in the carbon matrix from TEM images, the carbon matrices perform as conductive network for the electron transport. It can be seen from the SEM images that the carbon network formed from AC appears to favor better particle connectivity because the morphology of AC is finely divided pellets, while for CNT network and graphite nanosheet matrix, the intersection points or contact areas between the particles are much less than those in AC matrix. The high surface-to-volume ratio and more connections of

$\text{Na}_3\text{V}_2(\text{PO}_4)_3/\text{AC}$ ensures continuous pathways for electrons and better contact with electrolyte, hence improve the electronic conductivities and contribute to rate performance. This can be certified from the EIS measurement that the charge-transfer resistance of $\text{Na}_3\text{V}_2(\text{PO}_4)_3/\text{AC}$ is much smaller than that of $\text{Na}_3\text{V}_2(\text{PO}_4)_3/\text{CNT}$ and $\text{Na}_3\text{V}_2(\text{PO}_4)_3/\text{graphite}$. The shorter intercalation distance for Na^+ ions and better conductive pathways for electrons in the AC enable the higher sodium flux across the interface, and the best electrochemical performance can be achieved. Additionally, the AC spheres provide the robustness and buffers the stress and strain related to the particle volume expansion/contraction during the sodium intercalation/deintercalation, which are necessary to maintain the structure integrity as well as the cycling stability of $\text{Na}_3\text{V}_2(\text{PO}_4)_3/\text{AC}$.

In conclusion, NASICON-type $\text{Na}_3\text{V}_2(\text{PO}_4)_3$ nanograins dispersed in different carbon matrices were successfully synthesized via a facile method. Their performance in sodium half cells was compared and the mechanism of sodium diffusion pathways in different carbon matrix dimensions was investigated for the first time. $\text{Na}_3\text{V}_2(\text{PO}_4)_3$ nanograins dispersed in AC show the best electrochemical properties, thus making them a promising candidate for sodium-ion batteries. This material exhibits a discharge capacity of 117.5 mAh g^{-1} at 0.5 C in the initial stage, approximately 100% of the theoretical capacity of $\text{Na}_3\text{V}_2(\text{PO}_4)_3$ and a very stable cycling performance of 96.4% capacity retention at a 5 C rate over 200 cycles. Our as-synthesized material can be assembled into symmetric sodium-ion batteries, and $\text{Na}_3\text{V}_2(\text{PO}_4)_3/\text{AC}$ in the symmetric batteries exhibits excellent performance of 80% capacity retention after 200 cycles at 1 C, and can tolerate a very high current rate of 10 C. This superior performance may be attributed to the 3D sodium intercalation/deintercalation pathways and electron transport, which provides a significantly easier sodium path and better conductivity compared with $\text{Na}_3\text{V}_2(\text{PO}_4)_3/\text{CNT}$ and $\text{Na}_3\text{V}_2(\text{PO}_4)_3/\text{graphite}$. Moreover, the 3D carbon framework provides the robustness for the structure during cycling, thus endows this material with excellent cycling performance. Owing to the simple synthesis of the high-performance $\text{Na}_3\text{V}_2(\text{PO}_4)_3/\text{carbon}$ material, it is expected to be used in a wide range of applications in next-generation rechargeable batteries. The demonstrated symmetric sodium-ion battery performance with improved safety, longer lifetime, ability of charging in both directions, and lower cost due to utilizing the same material for both the cathode and the anode will also provide many opportunities to outclass other competitor systems for operation in the fields of energy storage and transportation.

Experimental Section

Synthesis: NH_4VO_3 , H_3PO_4 and Na_2CO_3 were analytical grade reagents, graphite was chemically pure and they were all purchased from the Sinopharm Chemical Reagent Co., Ltd. (Shanghai, China). Carbon nanotubes were chemically pure and purchased from Xianfeng Nano Inc. (Nanjing, China). Acetylene Black was chemically pure and purchased from Shanghai Chemical Reagent Co., Ltd. (Shanghai, China). All chemicals were used directly without any further treatment. NH_4VO_3 , H_3PO_4 , Na_2CO_3 and acetylene carbon were used as starting materials and NH_4VO_3 , H_3PO_4 , Na_2CO_3 were in a molar ratio of 2:3:1.5. Firstly, H_3PO_4 was slowly introduced into the NH_4VO_3 solution dropwise under

magnetic stirring. When a brownish-red solution was formed, Na_2CO_3 , and acetylene carbon were added into the solution and stirred for 20 min. The mixture was continuously stirred at 70 °C for 7 h to form a homogeneous suspension. Then, the solution was dried at 70 °C in air oven and pre-heated at 300 °C for 4 h in Ar atmosphere. Finally, the pre-heated material was ground and sintered at 800 °C for 8 h under Ar flow to yield $\text{Na}_3\text{V}_2(\text{PO}_4)_3/\text{AC}$ composite. For $\text{Na}_3\text{V}_2(\text{PO}_4)_3/\text{CNT}$ and $\text{Na}_3\text{V}_2(\text{PO}_4)_3/\text{graphite}$, the acetylene carbon was replaced by CNTs and graphite, respectively.

Characterization: X-ray diffraction (XRD) measurement was performed to investigate the crystallographic information using a Bruker D8 Advance X-ray diffractometer with a non-monochromated $\text{Cu K}\alpha$ X-ray source. Scanning electron microscopic (SEM) images and energy dispersive X-ray spectra (EDS) were collected with a JEOL JSM-7100F SEM/EDS microscope at an acceleration voltage of 15 kV. Transmission electron microscopic (TEM) and high resolution transmission electron microscopic (HRTEM) images were recorded with a JEOL JEM-2100F STEM/EDS microscope. The element analyses were performed by a Elementar Vario EL cube elemental analyzer. Bräuer-Emmert-Teller surface area was measured using Tristar II 3020 instrument by adsorption of nitrogen at 77 K.

Electrochemical characterization: The electrochemical properties were measured with 2025 coin cells assembled in a glove box filled with pure argon gas. In sodium half cells, sodium metal was used as the anode, a 1 M solution of NaClO_4 in ethylene carbon (EC)-dimethyl carbonate (DMC) (1:2 w/w) was used as the electrolyte, and Whatman Glass Microfibre Filter (Grade GF/F) was used as separator. The cathode electrodes were produced with 70% $\text{Na}_3\text{V}_2(\text{PO}_4)_3/\text{C}$ composites active material, 20% carbon black and 10% poly(tetrafluoroethylene), the active material content in the electrode was around 3.0 mg. Galvanostatic charge-discharge measurement was performed in the potential range of 2.3 to 3.9 V vs. Na/Na^+ with a multi-channel battery testing system (LAND CT2001A). Cyclic voltammetry (CV) and electrochemical impedance spectra (EIS) were measured by an electrochemical workstation (Autolab PGSTAT 302 and CHI 760D). In symmetric sodium-ion battery test, the battery was assembled into a laminated-type full cell and was cathode limited with as-prepared $\text{Na}_3\text{V}_2(\text{PO}_4)_3/\text{carbon}$ as both cathode and anode. Specific energy E (Wh kg^{-1}) can be calculated by $E = \int_0^{t_0} \frac{V}{m} V(t) dt$, where t is the discharge time, I_0 (A) is the constant current, m (kg) is the mass of the active material, and $V(t)$ is the time-dependent voltage in the dimension of V. Specific power P (W kg^{-1}) can be calculated by $P = E/t$.

Supporting Information

Supporting Information is available from the Wiley Online Library or from the author.

Acknowledgements

This work was supported by the the International Science & Technology Cooperation Program of China (2013DFA50840), the National Basic Research Program of China (2013CB934103, 2012CB933003), National Natural Science Foundation of China (51072153, 51272197) and the Fundamental Research Funds for the Central Universities (2012-yb-02, 2013-VII-028, 2013-ZD-7). Thanks to Prof. Dongyuan Zhao of Fudan University for his kind supervision, stimulating discussion and strong support. Thanks to Prof. C. M. Lieber of Harvard University and Dr. Jun Liu of Pacific Northwest National Laboratory for strong support and stimulating discussion.

Received: November 6, 2013

Revised: January 17, 2014

Published online: March 14, 2014

- [1] S. Chu, A. Majumdar, *Nature* **2012**, *488*, 294.
- [2] N. Armaroli, V. Balzani, *Angew. Chem. Int. Ed.* **2007**, *46*, 52.
- [3] P. Yang, J. M. Tarascon, *Nat. Mater.* **2012**, *11*, 560.
- [4] J. Liu, *Adv. Funct. Mater.* **2013**, *23*, 924.
- [5] M. M. Thackeray, C. Wolverton, E. D. Isaacs, *Energy Environ. Sci.* **2012**, *5*, 7854.
- [6] B. Dunn, H. Kamath, J. M. Tarascon, *Science* **2011**, *334*, 928.
- [7] M. Armand, J. M. Tarascon, *Nature* **2008**, *451*, 652.
- [8] M. S. Whittingham, *Chem. Rev.* **2004**, *104*, 4271.
- [9] S. Li, Y. F. Dong, D. D. Wang, W. Chen, L. Huang, C. W. Shi, L. Q. Mai, *Front. Phys.* **2013**, DOI: 10.1007/s11467-013-0343-7.
- [10] Y. Gogotsi, P. Simon, *Science* **2011**, *334*, 917.
- [11] L. Q. Mai, Q. L. Wei, Q. Y. An, X. C. Tian, Y. L. Zhao, X. Xu, L. Xu, L. Chang, Q. J. Zhang, *Adv. Mater.* **2013**, *25*, 2969.
- [12] F. Y. Cheng, J. Liang, Z. L. Tao, J. Chen, *Adv. Mater.* **2011**, *23*, 1695.
- [13] N. S. Choi, Z. Chen, S. A. Freunberger, X. Ji, Y. K. Sun, K. Amine, G. Yushin, L. F. Nazar, J. Cho, P. G. Bruce, *Angew. Chem. Int. Ed.* **2012**, *51*, 9994.
- [14] J. M. Tarascon, M. Armand, *Nature* **2001**, *414*, 359.
- [15] T. H. Kim, J. S. Park, S. K. Chang, S. Choi, J. H. Ryu, H. K. Song, *Adv. Energy Mater.* **2012**, *2*, 860.
- [16] H. Zhou, *Energy Environ. Sci.* **2013**, *6*, 2256.
- [17] S. P. Ong, V. L. Chevrier, G. Hautier, A. Jain, C. Moore, S. Kim, X. Ma, G. Ceder, *Energy Environ. Sci.* **2011**, *4*, 3680.
- [18] S. W. Kim, D. H. Seo, X. Ma, G. Ceder, K. Kang, *Adv. Energy Mater.* **2012**, *2*, 710.
- [19] V. Palomares, M. Casas-Cabanas, E. Castillo-Martínez, M. H. Han, T. Rojo, *Energy Environ. Sci.* **2013**, *6*, 2312.
- [20] N. Yabuuchi, M. Kajiyama, J. Iwatate, H. Nishikawa, S. Hitomi, R. Okuyama, R. Usui, Y. Yamada, S. Komaba, *Nat. Mater.* **2012**, *11*, 512.
- [21] L. Wang, Y. Lu, J. Liu, M. Xu, J. Cheng, D. Zhang, J. B. Goodenough, *Angew. Chem. Int. Ed.* **2013**, *52*, 1964.
- [22] V. Palomares, P. Serras, I. Villaluenga, K. B. Hueso, J. Carretero-González, T. Rojo, *Energy Environ. Sci.* **2012**, *5*, 5884.
- [23] C. Luo, Y. Xu, Y. Zhu, Y. Liu, S. Zheng, Y. Liu, A. Langrock, C. Wang, *ACS Nano* **2013**, *7*, 8003.
- [24] A. Rudola, S. Kuppan, S. Devaraj, H. Gong, P. Balaya, *Chem. Commun.* **2013**, *49*, 7451.
- [25] P. Senguttuvan, G. Rousse, V. Seznec, J.-M. Tarascon, M. R. Palacin, *Chem. Mater.* **2011**, *23*, 4109.
- [26] K. H. Ha, S. H. Woo, D. Mok, N. S. Choi, Y. Park, S. M. Oh, Y. Kim, J. Kim, J. Lee, L. F. Nazar, *Adv. Energy Mater.* **2013**, *3*, 770.
- [27] A. Darwiche, C. Marino, M. T. Sougrati, B. Fraisse, L. Stieveno, L. Monconduit, *J. Am. Chem. Soc.* **2012**, *134*, 20805.
- [28] D. Kim, S. H. Kang, M. Slater, S. Rood, J. T. Vaughey, N. Karan, M. Balasubramanian, C. S. Johnson, *Adv. Energy Mater.* **2011**, *1*, 333.
- [29] Y. L. Cao, L. F. Xiao, W. Wang, D. W. Choi, Z. M. Nie, J. G. Yu, L. V. Saraf, Z. G. Yang, J. Liu, *Adv. Mater.* **2011**, *23*, 3155.
- [30] Y. Sun, L. Zhao, H. Pan, X. Lu, L. Gu, Y.-S. Hu, H. Li, M. Armand, Y. Ikuhara, L. Chen, X. Huang, *Nat. Commun.* **2013**, *4*, 1870.
- [31] Y. U. Park, D. H. Seo, H. S. Kwon, B. Kim, J. Kim, H. Kim, I. Kim, H. I. Yoo, K. Kang, *J. Am. Chem. Soc.* **2013**, *135*, 13870.
- [32] H. Zhu, Z. Jia, Y. Chen, N. J. Weadock, J. Wan, O. Vaaland, X. Han, T. Li, L. Hu, *Nano Lett.* **2013**, *30*, 3093.
- [33] L. Chen, Q. Gu, X. Zhou, S. Lee, Y. Xia, Z. Liu, *Sci. Rep.* **2013**, *3*, 1946.
- [34] A. Ponrouch, E. Marchante, M. Courty, J. M. Tarascon, M. R. Palacin, *Energy Environ. Sci.* **2012**, *5*, 8572.
- [35] K. Sakaushi, E. Hosono, G. Nickerl, T. Gemming, H. Zhou, S. Kaskel, J. Eckert, *Nat. Commun.* **2013**, *4*, 1485.
- [36] Y. Liu, Y. Xu, Y. Zhu, J. N. Culver, C. A. Lundgren, K. Xu, C. Wang, *ACS Nano* **2013**, *7*, 3627.

- [37] Y. Kim, Y. Park, A. Choi, N. S. Choi, J. Kim, J. Lee, J. H. Ryu, S. M. Oh, K. T. Lee, *Adv. Mater.* **2013**, *25*, 3045.
- [38] H. Pan, Y. S. Hu, L. Chen, *Energy Environ. Sci.* **2013**, *6*, 2338.
- [39] R. Tripathi, S. Wood, M. S. Islam, L. Nazar, *Energy Environ. Sci.* **2013**, *6*, 2257.
- [40] K. T. Lee, S. Y. Hong, Y. Kim, Y. Won Park, A. Choi, N. S. Choi, *Energy Environ. Sci.* **2013**, *6*, 2067.
- [41] H. Pan, X. Lu, X. Yu, Y. S. Hu, H. Li, X. Q. Yang, L. Chen, *Adv. Energy Mater.* **2013**, *3*, 1186.
- [42] B. L. Ellis, L. F. Nazar, *Curr. Opin. Solid State Mater. Sci.* **2012**, *16*, 168.
- [43] C. Masquelier, L. Croguennec, *Chem. Rev.* **2013**, *113*, 6552.
- [44] M. D. Slater, D. Kim, E. Lee, C. S. Johnson, *Adv. Funct. Mater.* **2012**, *23*, 947.
- [45] L. Q. Mai, S. Li, Y. F. Dong, Y. L. Zhao, Y. Z. Luo, H. M. Xu, *Nanoscale* **2013**, *5*, 4864.
- [46] J. Goodenough, H. P. Hong, J. Kafalas, *Mater. Res. Bull.* **1976**, *11*, 203.
- [47] J. Gopalakrishnan, K. K. Rangan, *Chem. Mater.* **1992**, *4*, 745.
- [48] S. Y. Lim, H. Kim, R. Shakoor, Y. Jung, J. W. Choi, *J. Electrochem. Soc.* **2012**, *159*, A1393.
- [49] Z. Jian, W. Han, X. Lu, H. Yang, Y. S. Hu, J. Zhou, Z. Zhou, J. Li, W. Chen, D. Chen, L. Chen, *Adv. Energy Mater.* **2012**, *3*, 156.
- [50] J. Kang, S. Baek, V. Mathew, J. Gim, J. Song, H. Park, E. Chae, A. K. Rai, J. Kim, *J. Mater. Chem.* **2012**, *22*, 20857.
- [51] K. Saravanan, C. W. Mason, A. Rudola, K. H. Wong, P. Balaya, *Adv. Energy Mater.* **2012**, *3*, 444.
- [52] P. Senguttuvan, G. Rousse, M. E. Arroyo y de Dompablo, Hervé Vezin, J.-M. Tarascon, M. R. Palacín, *J. Am. Chem. Soc.* **2013**, *135*, 3897.
- [53] L. S. Plashnitsa, E. Kobayashi, Y. Noguchi, S. Okada, J. I. Yamaki, *J. Electrochem. Soc.* **2010**, *157*, A536.
- [54] S.-C. Yin, H. Grondey, P. Strobel, M. Anne, L. F. Nazar, *J. Am. Chem. Soc.* **2003**, *125*, 10402.
- [55] S. Komaba, W. Murata, T. Ishikawa, N. Yabuuchi, T. Ozeki, T. Nakayama, A. Ogata, K. Gotoh, K. Fujiwara, *Adv. Funct. Mater.* **2011**, *21*, 3859.
- [56] K. Du, H. Guo, G. Hu, Z. Peng, Y. Cao, *J. Power Sources* **2013**, *223*, 284.
- [57] J. N. Son, S. H. Kim, M. C. Kim, K. J. Kim, V. Aravindan, W. I. Cho, Y. S. Lee, *J. Appl. Electrochem.* **2013**, *43*, 583.
- [58] Z. Jian, L. Zhao, H. Pan, Y. S. Hu, H. Li, W. Chen, L. Chen, *Electrochem. Commun.* **2012**, *14*, 86.
- [59] C. Ponce de Leon, A. Frías-Ferrer, J. González-García, D. Szánto, F. C. Walsh, *J. Power Sources* **2006**, *160*, 716.
- [60] S. Wenzel, T. Hara, J. Janek, P. Adelhelm, *Energy Environ. Sci.* **2011**, *4*, 3342.